Strong Exciton-Photon Coupling in an Organic Single Crystal Microcavity

S Kéna-Cohen,[1,2] M. Davanço,[2] and S. R. Forrest[2,*]

[1]*Princeton Institute for the Science and Technology of Materials (PRISM), Department of Electrical Engineering, Princeton University, Princeton, New Jersey 08544, USA*

[2]*Departments of Electrical Engineering and Computer Science and Physics, University of Michigan, Ann Arbor, Michigan 48109, USA*

(Received 30 March 2008; revised manuscript received 11 July 2008; published 9 September 2008)

We demonstrate strong exciton-photon coupling of Frenkel excitons at room temperature in a microcavity composed of a melt grown thin film anthracene single crystal and two distributed Bragg reflectors. Angle-resolved reflectivity and normal incidence photoluminescence under weak excitation are observed. The microcavity spectrum is a function of the anisotropy of the crystalline material and the strong exciton-photon coupling of the excitonic resonances to the cavity photon. The photoluminescence spectrum is found to be completely polarized along the crystal axes.

DOI: 10.1103/PhysRevLett.101.116401 PACS numbers: 71.36.+c, 78.66.Qn

Strong exciton-photon coupling is attained when the light-matter interaction is stronger than the dissipative widths of the interacting particles. In inorganic semiconductor microcavities, there has been great interest in the strong coupling regime with the recent demonstration of Bose-Einstein condensation (BEC) of cavity polaritons: the coupled cavity photon-exciton eigenstates [1,2]. Although organic semiconductor-based microcavities exhibiting large Rabi splittings at room temperature were first demonstrated a decade ago [3,4], to our knowledge, there has yet to be a demonstration of parametric amplification or polariton condensation in these systems. The demonstration of such effects will provide a route for the fabrication of low-cost, tunable, polariton-based devices such as electrically pumped organic polariton lasers [5].

Most of the strongly coupled organic semiconductor microcavities reported to date have been composed either of disordered mixtures of J aggregates in a host matrix [3] or of thermally evaporated amorphous small-molecular weight films [6,7]. Here we present a paradigm shift in the design and fabrication of organic microcavities: A *single crystal* organic microcavity is fabricated using a technique that provides nanometer-thickness control of the cavity length. Indeed, microcavities containing organic single crystals are highly desirable for the realization of polariton BEC and other nonlinear optical phenomena due to their high degree of structural order, high damage threshold, and increased exciton-exciton interaction.

We find that the excitation spectrum is significantly modified for the crystalline microcavity, most importantly by the appearance of a second lower polariton branch and a dependence of the dispersion on sample orientation. In addition, the polaritons now couple both s and p cavity photons resulting in linearly polarized excitations along each crystal axis. Indeed, these properties have been predicted theoretically [8,9], and the second branch has been experimentally observed in a polycrystalline thin film of tetracene [10]. In that case, however, the measured dispersion was an average over the randomly oriented domains contained within the excitation region.

In disordered, or inhomogenously broadened microcavities with weak intermolecular interaction, the majority of the excitations are localized molecular excitations [11]. Plane-wave-like, or ''coherent,'' polaritons are limited to only a restricted region in k space [11]. Crystalline microcavities, however, are homogenously broadened, and the fraction of coherent polaritons can be greatly increased by reducing the temperature and thus the excitonic linewidth. Moreover, the cavity quality factor (Q) of organic microcavities has typically been lower than for their inorganic counterparts due to the difficulties associated with fabricating high quality dielectric Bragg reflectors (DBRs) on the top of soft organic materials.

Here anthracene, an archetypical polyacene, is used as a cavity material because of its high quantum yield [12] (0.99) and damage threshold. A high cavity quality factor is achieved by avoiding direct deposition of dielectric mirrors over the organic material. All of the measurements in this Letter were taken at room temperature.

The fabricated structure, shown in the inset in Fig. 1, is composed of 30 mm-long $\times$ 0.5 mm-wide $\times$ 140 nm-thick anthracene single crystal channels sandwiched between two DBRs composed of 12, alternating $\lambda/4$ pairs of SiO_2/SiN_x. The microcavity was fabricated in three steps. First, the DBRs were grown on quartz substrates by plasma-enhanced chemical vapor deposition. Then 70 nm-thick, 0.5 mm-wide gold stripes, separated by 0.5 mm-wide gaps, were defined along the length of the substrate using photolithography and lift-off. Two substrates were then put together such that the DBRs were positioned face to face with their gold stripes aligned. Application of pressure caused portions of the gold stripes to cold weld, holding the substrates together. The cold welding process was then completed by applying 75 MPa of pressure with a mechanical press for 30 s. This resulted in approximately 140 nm-thick, ''empty'' microcavity

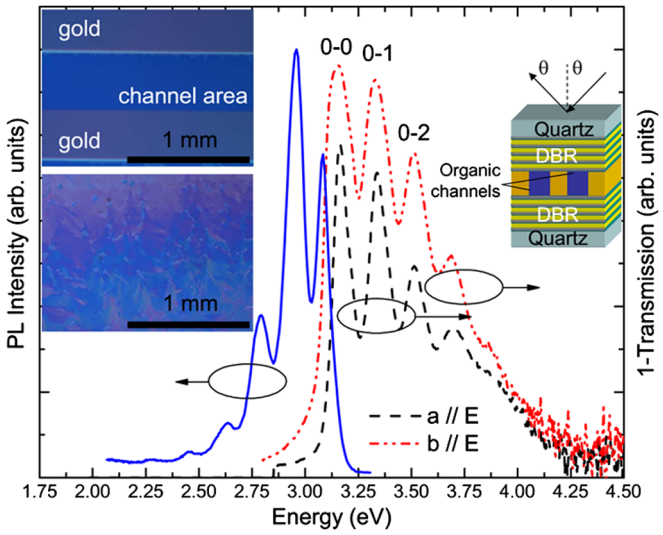

FIG. 1 (color online). Right: Inverse transmission (1-T) spectrum of a 120 nm-thick anthracene single crystal channel for electric field polarizations along the **a** and **b** crystal axes. Because of the large oscillator strength of the first singlet transition in anthracene, there is significant reflection at resonance, and the transmission cannot be taken as a direct measure of the absorption. Left: Photoluminescence spectrum of a 120 nm-thick anthracene single crystal (uncorrected for self-absorption). The vibronic replicas mirror the absorption spectrum, with the highest energy peak distorted by self-absorption. Right inset: Schematic of the fabricated microcavity structure. Left insets: Phase contrast micrographs of the channel area from the completed structure (top) and a thicker area far away from the gold channels where multiple domains can be observed (bottom). The scale bar is 1 mm.

channels. The bonded sample was placed in a Pyrex Petri dish partially filled with anthracene. Upon melting in a nitrogen atmosphere at 240 °C, liquid anthracene penetrated the channels by capillary action and was crystallized by decreasing the temperature at a rate of $\sim 1\,^{\circ}\mathrm{C}/\mathrm{min}$. The crystallization process was found to depend heavily on the gap thickness and cooling rate. For small gaps ($<3\ \mu$m thick) and slow cooling ($<1.5\,^{\circ}\mathrm{C}/\mathrm{min}$), the process reproducibly yielded larger than centimeter-sized anthracene single crystals. Figure 1 shows phase contrast micrographs of the channel area taken both from the finished structure and from a polycrystalline area far away from the channels. No contrast is observed within the channel region. The single crystal nature of the films was also confirmed by the rotational dependence of the reflection high energy electron diffraction patterns and the appearance of Kikuchi lines [13]. X-ray diffraction on separated slides confirmed that, in all cases, the crystals were found to have **a** and **b** crystal axes lying in plane. For most of the channels, the **b** axis was found to lie along or very nearly along the channel length. The melting process itself has been described in more detail elsewhere [14,15] but in those cases was found to result in uncontrolled thicknesses in the micrometer range. Concurrent with our work, evidence for strong coupling in a similar structure was obtained via transmission through a sample of uncontrolled thickness [16]. Here reproducible thickness control on the nanometer scale allows for the unambiguous interpretation of the polariton dispersion.

The (inverted) transmission spectrum of a 120 nm-thick anthracene crystal grown from the melt is shown in Fig. 1, with the electric field vector **E** polarized along both the **a** and **b** crystal axes. Peaks in the spectra correspond to transitions from the ground state to the intermolecular vibronics of the first excited singlet state. From the transmission spectrum, the 0-0 transition energy along the **b** crystal axis is seen to be slightly redshifted compared to that along the **a** crystal axis. The splitting between these two transitions occurs due to the resonant Coulomb interaction between the two molecules forming the anthracene unit cell and is referred to as the Davydov splitting [17]. The splitting is $\sim 200\ \mathrm{cm}^{-1}$ for the 0-0 transition [18], which is smaller than the homogenous linewidth at room temperature. As a result, the redshift is difficult to resolve in transmission. Most of the oscillator strength, however, is located along the **b** axis [18] resulting in significant changes in the microcavity spectrum.

Angle-resolved reflectivity spectra of the microcavity structure are shown for *p*-polarized light in Fig. 2. Spectra are shown for two different sample orientations, one with **a** ∥ **E** and the other with the sample rotated 90° degrees such that **b** ∥ **E**. In both cases, three peaks are found to anticross around the 0-0, 0-1, and 0-2 vibronic resonances with increasing incident angle. These peaks are identified by arrows and are associated with the lower polariton (LP) and middle polariton (MP1 and MP2) branches. In contrast to the bare excitonic transitions, LP_a and LP_b are easily distinguished. They are separated by more than 70 meV due mostly to the difference in background refractive index along each crystal axis. We assign the third peak to a middle polariton rather than an upper polariton based on the oscillator strength of the 0-2

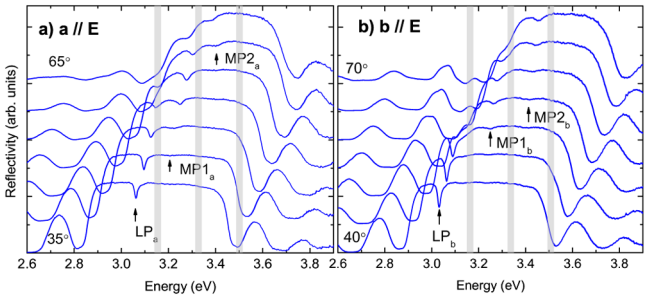

FIG. 2 (color online). The angle-dependent *p*-polarized reflectivity spectrum of a microcavity containing a 140 nm-thick anthracene crystal. The spectra are taken in 5° increments. The sample is oriented such that (a) the polarization and propagation direction is along **a** and (b) the polarization and propagation direction is along **b**. The lower polariton (LP) and middle polaritons (MP1 and MP2) are indicated by arrows. The gray lines indicate the energies of the bare resonances observed in the absence of a cavity.

vibronic and the observed flattening out of this branch with angle. We also observe an anticrossing of the DBR leaky mode [19] to the 0-0 transition for the sample oriented such that **b** ∥ **E**.

The dispersion extracted from the peak positions is shown in Fig. 3 for both *s* and *p* polarization with the sample oriented along either the **a** or the **b** crystal axis. The position of the *p*-polarized DBR sideband is also shown. From the plot, we see that, beyond $\theta = 60°$, both mirrors become transparent at the LP energy, and the LP ceases to exist. Also, *p* polarization was specifically chosen for Fig. 2 because of the difficulty in identifying the much weaker MP1 and MP2 dips for *s*-polarized light. Hence, only the LP branch dispersion is plotted in Fig. 3 for *s* polarization.

We observe large differences in the dispersions for *s*- and *p*-polarized light and for the two different sample orientations. Differences in the *s* and *p* dispersions occur due to the anisotropic polariton dispersion and the polarization splitting of the cavity mode. Even in the absence of anisotropy, a large polarization splitting can occur if the Fabry-Perot resonance defined by the cavity length differs significantly from the center of the DBR stop band. As the incidence angle increases, the DBR penetration depth increases for *p*-polarized light but decreases for *s*-polarized light, leading to a polarization splitting of the photon component of the cavity [20]. In our case, the polarization splitting was calculated to be $\Delta E_{\text{TM-TE}} = 0.11 \pm 0.02$ eV at 60°. At small angles, where the DBR penetration depths are nearly identical, differences between the *s*- and *p*-polarized reflectivity are due solely to anisotropy in the crystalline cavity material. Differences between Figs. 3(a) and 3(b), which result from rotating the sample, are also a result of the in-plane anisotropy.

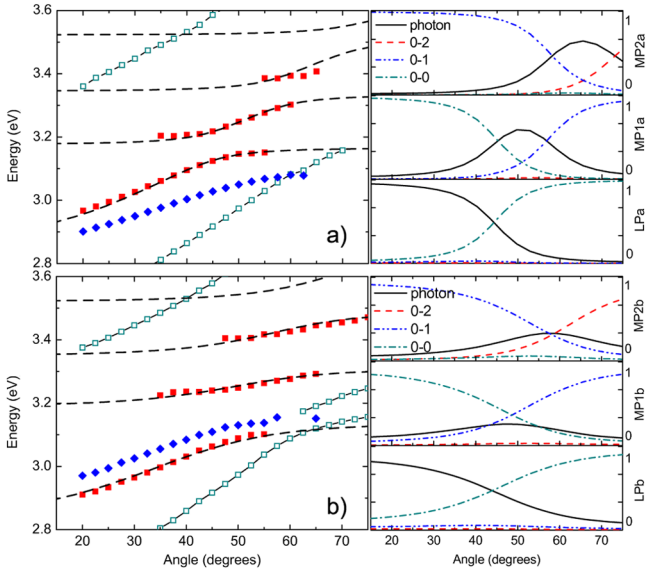

FIG. 3 (color online). Left: Dip positions extracted from *p*- (solid squares) and *s*-polarized (solid diamonds) reflectivity. The position of the DBR side band for *p* polarization is also indicated (open squares). The dashed lines are a fit to a 4-body coupled harmonic oscillator Hamiltonian. Right: Photonic and excitonic branch content for each polariton branch (*p* polarization). The data are shown for the sample oriented such that (a) the *p* polarization is along **a** and (b) the *p* polarization is along **b**.

The polariton dispersion from Fig. 3 can be modeled by a coupled harmonic oscillator Hamiltonian:

$$\begin{pmatrix} E_{\text{ph}}(\theta) & V_1 & V_2 & V_3 \\ V_1 & E_{\text{ex0-0}} & 0 & 0 \\ V_2 & 0 & E_{\text{ex0-1}} & 0 \\ V_3 & 0 & 0 & E_{\text{ex0-2}} \end{pmatrix} \begin{pmatrix} \alpha \\ \beta \\ \chi \\ \delta \end{pmatrix} = E \begin{pmatrix} \alpha \\ \beta \\ \chi \\ \delta \end{pmatrix}. \quad (1)$$

Interaction potentials (V_1, V_2, and V_3) and uncoupled exciton energies ($E_{\text{ex0-0}}$, $E_{\text{ex0-1}}$, and $E_{\text{ex0-2}}$) are included for the three lowest intermolecular vibronics [21]. The cavity photon dispersion is given by

$$E_{\text{ph}}(\theta) = E_{\text{ph}}(0)\left(1 - \frac{\sin^2\theta}{n_{\text{eff}}}\right)^{-1/2}. \quad (2)$$

The parameters used in the resulting fit shown in Fig. 3 are summarized in Table I. The most striking differences between the two sets of parameters are the larger interaction potentials for the **b** exciton due to its larger oscillator strength. Much of the discrepancy from the fit comes from assuming a constant effective index n_{eff}, while, over the energy range spanned (1 eV), the true effective index should reflect dispersion in the DBR refractive indices and background cavity index [20]. Also, the error to the fit to V_3 is highest due to the absence of data points for the upper branch. The photonic $\{|\alpha|^2\}$ and excitonic $\{|\beta|^2, |\chi|^2, |\delta|^2\}$ weights for each branch are shown as insets in Fig. 3. Finally, it should be emphasized that this description is appropriate only for propagation along the crystal axis corresponding to the branch of interest. In general, we find that the dispersion depends on the *direction* of propagation.

It has been shown that, along a principal axis of a crystalline organic microcavity, the dispersion is uniquely determined by the excitonic component along that axis [8,9]. Off axis, however, the cavity photon couples both excitonic components, which leads to the appearance of additional branches. In Fig. 4, we show reflectivity spectra for the sample oriented such that **a** ∥ **E** for *p*-polarized light, **b** ∥ **E** for *s*-polarized light, and **E** oriented at 45° between the two axes. Single LP branches are identified for linear polarization along each crystal axis. For off-axis

TABLE I. Harmonic oscillator fit parameters[a].

Orientation	$E_{\text{ph}}(0)$ (eV)	n_{eff}	V_1 (meV)	V_2 (meV)	V_3 (meV)
$a \parallel E$	2.918 ± 0.006	1.73 ± 0.05	47 ± 5	43 ± 4	50 ± 30
$b \parallel E$	2.939 ± 0.006	1.74 ± 0.03	108 ± 2	94 ± 4	80 ± 10

[a]The uncoupled exciton energies that were kept fixed at $E_{0-0} = 3.17$ eV, $E_{0-1} = 3.34$ eV, and $E_{0-2} = 3.52$ eV for the **a** exciton and $E_{0-0} = 3.16$ eV, $E_{0-1} = 3.33$ eV, and $E_{0-2} = 3.51$ eV for the **b** exciton.

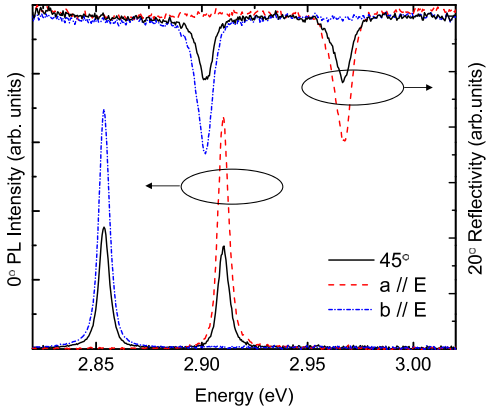

FIG. 4 (color online). Bottom: Normal incidence photoluminescence spectrum taken for three polarizer orientations. The excitation wavelength was $\lambda = 325$ nm. Top: 20° reflectivity spectrum with the sample aligned such that $\mathbf{a} \parallel \mathbf{E}$ for p polarization. The reflectivity is shown for 3 different polarizer orientations. In both cases, two LP branch peaks appear off-axis corresponding to both excitonic components.

polarization, however, both LP branches are observed, corresponding to the two excitonic components.

Photoluminescence (PL) at normal incidence was also measured using continuous-wave excitation from the $\lambda = 325$ nm line of a HeCd laser. The spectra are shown in Fig. 4. The sample was excited over a 100 μm spot at a power <25 μW. Only PL from the lower branches is observed. In contrast to the case of inorganic semiconductor microcavities, where the polaritons can be separated into s and p modes, we find that LP_a and LP_b are always linearly polarized along the **a** and **b** axes, respectively, regardless of the sample orientation with respect to the plane of incidence. A similar polarization anisotropy has also been reported in the PL of an aligned (rubbed) polymer film in a weakly coupled microcavity [22]. Moreover, the polarization dependence of the PL at normal incidence provides clear evidence of the single crystalline nature of the cavity material within the spot size.

The cavity quality factor Q can be measured from the LP linewidths at shallow angles, when the LP is mostly photonlike. From reflectivity measurements (~ 0.3 mm spot), linewidths of $\sim$7–9 meV are observed. Photoluminescence measurements yielded linewidths of $\sim$3.5–5.5 meV, corresponding to a lower bound of $Q \sim 800$. The measured linewidths are limited by averaging over the spot size. Indeed, by probing different spots on the sample, we find that the detuning can be varied by approximately 50 meV due to intrinsic variations in cavity thickness, possibly due to bowing of the channels, variations in bonding thickness, and incomplete cavity filling by anthracene, particularly around defects. As an upper bound estimate, we note that the calculated Q factor for this structure is $Q \sim 6000$, assuming perfectly flat DBR interfaces.

In conclusion, we have demonstrated strong exciton-photon coupling in an anthracene single crystal microcavity. The crystals were formed by allowing liquid anthracene to crystallize in controllable, nanometer-thick lithographically defined channels. The dispersion is found to reflect the anisotropy of the underlying crystalline material. It is characterized by the appearance of a second lower polariton branch and a dependence on sample orientation. In general, each branch consists of a mixture of Davydov components, photon polarizations, and the three lowest intermolecular vibronics. Photoluminescence which is polarized along the crystal axes is observed at normal incidence, and a lower bound of the cavity $Q = 800$ is measured. The crystalline nature of the cavity material, high Q factor, and low nonradiative losses make this structure an ideal candidate for the realization of polariton condensation in organic semiconductors.

This work was performed at the Lurie Nanofabrication Facility at the University of Michigan. The authors acknowledge Universal Display Corporation and the Air Force Office of Scientific Research for partial financial support. S. K.-C. acknowledges support from the Fonds Québecois sur la Nature et les Technologies.

*To whom correspondence should be addressed.
stevefor@umich.edu

[1] J. Kasprzak *et al.*, Nature (London) **443**, 409 (2006).
[2] R. Balili *et al.*, Science **316**, 1007 (2007).
[3] D. G. Lidzey *et al.*, Phys. Rev. Lett. **82**, 3316 (1999).
[4] D. G. Lidzey *et al.*, Nature (London) **395**, 53 (1998).
[5] J. H. Song *et al.*, Phys. Rev. B **69**, 235330 (2004).
[6] S. Kena-Cohen and S. R. Forrest, Phys. Rev. B **76**, 075202 (2007).
[7] R. J. Holmes and S. R. Forrest, Phys. Rev. B **71**, 235203 (2005).
[8] H. Zoubi and G. C. La Rocca, Phys. Rev. B **71**, 235316 (2005).
[9] M. Litinskaya, P. Reineker, and V. M. Agranovich, Phys. Status Solidi A **201**, 646 (2004).
[10] S. Kena-Cohen and S. R. Forrest, Phys. Rev. B **77**, 073205 (2008).
[11] V. M. Agranovich, M. Litinskaia, and D. G. Lidzey, Phys. Rev. B **67**, 085311 (2003).
[12] R. E. Kellogg, J. Chem. Phys. **44**, 411 (1966).
[13] R. R. Lunt, S. Kena-Cohen, and S. R. Forrest (to be published).
[14] H. Kondo *et al.*, J. Lumin. **119**, 137 (2006).
[15] S. Hashimoto, N. Ohno, and M. Itoh, Phys. Status Solidi B **165**, 277 (1991).
[16] H. Kondo *et al.*, J. Lumin. **128**, 777 (2008).
[17] A. S. Davydov, *Theory of Molecular Excitons* (Plenum, New York, 1971).
[18] G. C. Morris and M. G. Sceats, Chem. Phys. **3**, 164 (1974).
[19] M. Richard *et al.*, Appl. Phys. Lett. **86**, 071916 (2005).
[20] G. Panzarini *et al.*, Fiz. Tverd. Tela (Leningrad) **41**, 1337 (1999).
[21] R. J. Holmes and S. R. Forrest, Phys. Rev. Lett. **93**, 186404 (2004).
[22] T. Virgili *et al.*, Chem. Phys. Lett. **341**, 219 (2001).